Improving numerical accuracy for the viscous-plastic formulation of sea ice

Tongtong Li[a,1,*], Anne Gelb[a,1], Yoonsang Lee[a,1]

[a]*Department of Mathematics, Dartmouth College, Hanover, NH 03755, USA*

Abstract

Accurate modeling of sea ice dynamics is critical for predicting environmental variables and is important in applications such as navigating ice breaker ships, and as such there have been numerous investigations on modeling sea ice dynamics. The 1979 viscous-plastic (VP) sea ice model introduced by W.D. Hibler remains the most widely accepted. Due to its highly nonlinear features, the Hibler model is intrinsically challenging for computational solvers. This study therefore focuses on improving the numerical accuracy of the VP sea ice model. Since the poor convergence observed in existing numerical simulations stems from the nonlinear nature of the VP formulation, this investigation proposes using the celebrated weighted essentially non-oscillatory (WENO) scheme – as opposed to the frequently employed centered difference (CD) scheme – for the spatial derivatives in the VP sea ice model. We then proceed to numerically demonstrate that WENO yields higher-order convergence for smooth solutions, and that furthermore it is able to resolve the discontinuities in the sharp features of sea ice covers – something that is not possible using CD methods. Finally, our proposed framework introduces a potential function method that utilizes the phase field method that naturally incorporates the physical restrictions of ice thickness and ice concentration in transport equations, resulting in modified transport equations which include additional forcing terms. Our method does not require post-processing, thereby avoiding the possible introduction of discontinuities and corresponding negative impact on the solution behavior. Numerical experiments are provided to demonstrate the efficacy of our new methodology.

*Corresponding author

Email addresses: tongtong.li@dartmouth.edu (Tongtong Li), annegelb@math.dartmouth.edu (Anne Gelb), yoonsang.lee@dartmouth.edu (Yoonsang Lee)

[1]All authors are supported by the DoD grant MURI ONR #N00014-20-1-2595. AG is also supported in part by the grants NSF DMS #1912685 and AFOSR #FA9550-22-1-0411. YL is also supported by the grant NSF DMS #1912999.

Keywords: Sea ice simulation, viscous-plastic model, weighted essentially non-oscillatory scheme, potential function method

1. Introduction

Sea ice dynamics plays a vital role in shaping the ice cover in polar regions. Properly representing sea ice dynamics is crucial in predicting environmental variables and is important in a wide range of applications such as the navigation of ice breaker ships [1, 2]. The observations of the Arctic Ice Dynamics Joint Experiment (AIDJEX) significantly improved sea ice dynamics modeling in the 1970s [3]. Since then there has been an increased effort in modeling sea ice dynamics [4, 5, 6, 7, 8, 9]. The VP sea ice model introduced by Hibler [4] has become the most widely used approach for sea ice dynamics. The model consists of a nonlinear momentum equation and two transport equations, and is initially developed for meshes in the range of 100 kilometers. To solve the momentum equation at this spatial resolution, implicit time-stepping schemes are recommended [10] due to the nonlinear character of the momentum equation stemming from the viscous-plastic material law. As the standard Picard solver exhibits slow convergence, solvers such as Jacobian-free Newton-Krylov (JFNK) solver [11] have been developed to improve the numerical efficiency for solving the VP model. The Elastic-Viscous-Plastic (EVP) model proposed by Hunke and Dukowicz [5] avoids implicit methods altogether by relaxing the stability condition for an explicit time-stepping scheme.

With increasing mesh resolutions now available, it is becoming more apparent that the numerical solutions to the sea ice model resulting from either the VP or EVP formulation are not well resolved, and indeed there is a significant discrepancy with obtainable observations [12]. How much of this difference is attributable to modeling error, e.g. due to discrepancies in the atmospheric forcing term, and how much to the numerical approximation error remains an open question [13]. In this study we focus on improving the numerical accuracy of the sea ice representation based on the one-dimensional (1D) VP model which will be discussed in Section 2.

While there are many aspects of the VP model that merit investigation, our focus here is on two different but related issues: (1) the numerical efficacy of the computational methods used for solving the model, which includes a study on both accuracy and convergence; and (2) ensuring that the computational method observes physical constraints on the ice thickness and concentration. A key aspect in our investigation is to demonstrate the importance of high order spatial discretization operators. Therefore, as part of our study we solve the VP model using an *explicit* time-stepping

solver in order to isolate the associated error. We note that this is not the same as the traditional EVP model. For comparison purposes we run a simulation using the EVP model in Appendix A. Discussion on each issue as motivation for this investigation is provided below.

1.1. Numerical efficacy of the VP sea ice model

One goal of this investigation is to address the numerical simulation of the nonlinear VP sea ice model, specifically concerning the accuracy, stability, and efficiency. While many efforts have been made to improve the computational *efficiency* of sea ice model solvers, e.g. [11, 14, 5, 15], analysis of the corresponding *convergence* properties is lacking, and indeed many of these methods fail to converge[16]. We note that [16], which proposes and implements an iterated IMplicit-EXplicit (IMEX) time integration to solve the coupled sea ice model monolithically, does provide an analysis of the temporal convergence of the numerical solution. There it is demonstrated that a combination of the second-order Runge-Kutta method for the explicit time integration and a second-order backward difference method for the implicit integration of the momentum equation yields an overall second-order accuracy in time of the numerical solution when compared to a reference solution obtained using a tiny time step (1 second). Spatial convergence is investigated in [17], where it is shown that in the VP sea ice model, the simulated velocity field depends on the spatial resolution of the model and approaches the analytical solution as the spatial resolution is increased. However, the study is not quantified in terms of convergence rate. The method in [18, 19] adopts the Crank Nicholson time discretization and three point stencil centered difference (CD) spatial discretization together with the JFNK solver. By simultaneously refining both spatial and temporal resolutions, second-order convergence is sometimes observed for a specifically designed synthetic model. Convergence rates are estimated using the L_2 and L_∞ norms by computing solutions for two different mesh refinements at the end of each day during the 6-day simulation. We note that the mesh refinement does not consistently correspond to better accuracy for this simulated experiment, however.

To the best of our knowledge, convergence with respect to spatial resolution has not been well studied. In particular, no clear conclusion has been drawn in terms of spatial convergence. We adopt this as a starting point in our investigation to explore the related numerical properties. As we focus on spatial convergence, we choose the time step to be sufficiently small so that the time discretization error does not affect the convergence rate. This allows us to test the VP formulation using an explicit time-stepping scheme and therefore avoid the error caused by either the first-order

approximation to the Jacobian matrix or the corresponding prescribed stopping criterion in the nonlinear solver needed for the implicit time-stepping scheme. Based on a constructed analytical solution with appropriately added forcing term to the governing equations, we test for convergence on the VP sea ice model using both a second-order CD spatial discretization scheme as well as a third-order total variation diminishing (TVD) Runge-Kutta time integration scheme.

Nowadays, with increasing mesh resolutions, the general performance of the existing sea ice solvers is degrading, leading to a significant increase in numerical cost [3]. Higher-order spatial discretization methods may be able to offset this problem. Due to the natural discontinuity feature of ice thickness and concentration, traditional higher-order finite difference schemes typically have spurious oscillations near discontinuities (the Gibbs phenomenon), which may pollute smooth regions and even lead to instability, causing blowups of the schemes [20]. The weighted essentially non-oscillatory (WENO) method [21] is designed to achieve higher-order accuracy in smooth regions while sharply resolving discontinuities in an essentially non-oscillatory fashion. This study verifies that these desirable properties hold when implementing WENO for the sea ice model.

1.2. Ice thickness and ice concentration

Following the VP model by Hibler [4], two idealized thickness levels, namely thick and thin, are adopted to approximately characterize ice thickness in a relatively simple form. The two variables used to keep track of these levels are ice thickness, which is equivalent to the mass of ice in any grid cell, and ice concentration, which is defined as the fraction of the grid cell area covered by thick ice.

One issue is how the constraints on these two variables are imposed. In particular, assuming continuity of the ice thickness and the ice velocity, the ice thickness should remain non-negative (see [22, Theorem 3.10]). The non-negativity of ice concentration is similarly guaranteed. As will be demonstrated, preserving the non-negativity in both parameters is an important consideration for choosing a numerical solver. Moreover, although not explicitly providing a method to guarantee the upper bound of ice concentration to be 1, such a constraint is described in Hibler [4] to be equivalent to adding a mechanical sink term in the model, which is turned on when the ice concentration reaches 1 to prevent its further growth. A more formal derivation of the ice thickness distribution is given by Thorndike et al [23], in which more general thermodynamic processes and mechanical source and sink terms are considered. Yet the question still remains on how best to numerically incorporate physical constraints in models for which complicated forcing terms are already simplified. For

example, for short term predictions used for navigation purposes, there is likely a trade-off between efficiency and model consistency that has to be made.

More sophisticated ice thickness distribution models have been more recently introduced under the global climate model framework, such as the multi-thickness category model in CICE [24]. Despite these efforts, as far as we know, the numerical methods used to solve the model or impose the constraints have not been rigorously analyzed or compared. As already mentioned, the original work in [4] does not explicitly discuss how these constraints may be incorporated into the numerical implementation of the model under simplified source and sink terms. Since then some investigations have explicitly provided approaches both for numerical simulation of the model as well as for imposing these constraints. For example, Mehlmann [25] uses a finite element framework to solve the sea ice model and imposes restrictions on the trial spaces of ice thickness and concentration through a projection of the solution. Lipscomb and Hunke [26] adopt an incremental remapping scheme for sea ice transport. This is a Lagrangian approach that preserves the monotonicity by Van Leer limiting. That is, the gradients are reduced when necessary to ensure that the values in the reconstructed fields stay inside the range of the mean values in the cell and its neighbors. All of these mentioned approaches impose the model constraints through a post-processing procedure, which may, unfortunately, introduce discontinuity into the numerical solution, which affects the accuracy and might ultimately impact stability so that the solution does not converge.

Therefore, the other goal of this investigation is to develop a numerical approach that more intuitively imposes the model constraints without any post-processing procedure based on Hibler's model [4]. To accomplish this task, we propose using the potential function method motivated by the analogous approach of using a double-well potential function in what is commonly referred to as the phase field method [27, 28], which is designed to solve interface problems by treating the interface as an object with finite thickness. Our proposed method, described in Section 4, offers a simple but elegant way to incorporate additional restrictions into the model and could be generalized in various settings, such as the transport equations in other sea ice models. It further yields a modified transport model with the extra forcing terms coming from the potential energy function, which is consistent with Hibler's statement on how to include the mechanical sink term in the model.

The rest of the paper is organized as follows. In Section 2 we describe the sea ice model. Section 3 provides a brief overview of standard numerical solvers for the sea ice model, focusing on

the JFNK solver and the EVP model, as well as their adapted versions to the 1D VP model for the purpose of this investigation. We then describe our proposed approach, which includes both the WENO scheme and the potential function method in Section 4. In Section 5 we conduct some numerical experiments, illustrating and comparing the performances of our proposed approach with that of more typically employed methodology. We give some concluding remarks in Section 6.

2. Sea ice dynamics model

We begin by describing the two-dimensional (2D) VP model introduced by Hibler [4] for the simulation of sea ice circulation and thickness. Although sea ice dynamics occurs in a three-dimensional space, the vertical scale of $\mathcal{O}$(m) is much smaller than the horizontal scale of $\mathcal{O}$(1000 m), so the motion of sea ice is usually described in two dimensions. The VP sea ice model comprises of a momentum equation and two transport equations that describe the balance laws and is given by

$$m\frac{D\mathbf{u}}{Dt} = m(\frac{\partial \mathbf{u}}{\partial t} + \mathbf{u}\cdot\nabla\mathbf{u}) = \nabla\cdot\boldsymbol{\sigma} - mf\,\mathbf{k}\times\mathbf{u} + \boldsymbol{\tau}_a - \boldsymbol{\tau}_w - mg\nabla H_d, \tag{2.1a}$$

$$\frac{\partial h}{\partial t} + \nabla\cdot(\mathbf{u}\,h) = S_h, \tag{2.1b}$$

$$\frac{\partial A}{\partial t} + \nabla\cdot(\mathbf{u}\,A) = S_A. \tag{2.1c}$$

Here $\mathbf{u}$ is the 2D ice velocity, h is the mean ice thickness, A is the ice concentration. The ice mass per unit area m is given by ρh, where ρ is the sea ice density. The internal ice stress is denoted by $\boldsymbol{\sigma}$. The external forces comprise of the Coriolis force, forces due to air and water stress $\boldsymbol{\tau}_a$ and $\boldsymbol{\tau}_w$, and the ocean tilt stemming from the changing sea surface height. The other parameters include f the Coriolis parameter, $\mathbf{k}$, a unit vector perpendicular to the horizontal plane, g the acceleration due to gravity, and H_d the sea surface dynamic height. Finally, S_h and S_A are the thermodynamic source or sink terms. We note that the advection term $\mathbf{u}\cdot\nabla\mathbf{u}$ of ice momentum can be neglected due to scaling properties [29]. Furthermore, the thermodynamic terms are set to zero in the simulations as we concentrate on dynamic effects. The independent variables t and x are measured in seconds (s) and meters (m) correspondingly.

To better understand and analyze how well different computational approaches are suited to sea ice dynamics, we focus on a simplified 1D sea ice model in this study, which is given by

$$\rho h\frac{\partial u}{\partial t} - \tau_a + \tau_w - \frac{\partial \sigma}{\partial x} = 0, \tag{2.2a}$$

$$\frac{\partial h}{\partial t} + \frac{\partial}{\partial x}(u\,h) = 0, \tag{2.2b}$$

$$\frac{\partial A}{\partial t} + \frac{\partial}{\partial x}(u\,A) = 0. \tag{2.2c}$$

Here u is the 1D sea ice velocity and σ is the internal stress corresponding to $\boldsymbol{\sigma}_{xx}$ in the 2D model. We note that the Coriolis force and sea surface tilt are set to zero as the external forces act only in one direction on a static ocean slab [30, 17]. The air and water stress terms, τ_a and τ_w respectively, are determined from the nonlinear boundary layer theories and the quadratic drag formulas used in the model [31]:

$$\tau_a = \rho_a C_{da} |u_a| u_a, \tag{2.3}$$

$$\tau_w = \rho_w C_{dw} \sqrt{u^2 + \epsilon_1} u, \tag{2.4}$$

where ρ_a and ρ_w are the air and water densities, C_{da} and C_{dw} are the air and water drag coefficients, u_a is the surface wind, and ϵ_1 is a very small value (10^{-10} m^2/s^2) introduced for numerical stability. Here the sea ice drift speed is neglected in the air drag formulation as it is much slower than the wind speed. The water under the ice is assumed to be at rest, leading to the absence of the water velocity in the water drag formulation.

We now describe the rheology term modeling the ice interaction, a viscous-plastic constitutive law relating the stresses and the strain rates. Due to the dimension reduction, all other mixed derivative components $\boldsymbol{\sigma}_{xy}$, $\boldsymbol{\sigma}_{yx}$ and $\boldsymbol{\sigma}_{yy}$ vanish, and therefore the divergence of the stress tensor in (2.2a) is reduced to

$$\frac{\partial \sigma}{\partial x} = \frac{\partial}{\partial x}\left[(\eta + \zeta)\frac{\partial u}{\partial x} - \frac{P}{2}\right], \tag{2.5}$$

where

$$\eta = \zeta e^{-2} \quad \text{and} \quad \zeta = \frac{P}{2\Delta} \tag{2.6}$$

are the bulk and shear viscosities modeled by a normal flow rule in the plastic state and are chosen as constant values in the viscous regime. Here e is the eccentricity of the elliptical yield curve, and Δ in one dimension is obtained as

$$\Delta = \left[(1 + e^{-2})\left((\frac{\partial u}{\partial x})^2 + \epsilon_2\right)\right]^{1/2}, \tag{2.7}$$

with $\epsilon_2 = 10^{-22}$ s^{-2} as another small parameter introduced for numerical stability purposes.

The viscous coefficients in the VP formulation [4] are capped to prevent them from becoming arbitrarily large. This leads to a rheology term that is not continuously differentiable with respect

to velocity. To obtain a smooth formulation of the viscous coefficients, we follow Lemieux and Tremblay [13] and replace the expression of ζ by the hyperbolic tangent function

$$\zeta = \frac{P}{2\Delta_{\min}} \tanh(\frac{\Delta_{\min}}{\Delta}), \tag{2.8}$$

with $\Delta_{\min} = 2 \times 10^{-9}$ s^{-1} in accordance with the $\zeta_{\max}$ definition in [4].

The ice strength P is expressed as

$$P = P^{\star} h \exp[-C(1 - A)], \tag{2.9}$$

where $P^{\star}$ and C are the strength and concentration parameters.

Finally, Table 1 provides the values for all of the physical parameters which we will use in our numerical experiments. These parameter values are typically used in the VP sea ice model [14, 16, 32].

Symbol	Definition	Value
ρ	Sea ice density	900 kg/m^3
ρ_a	Air density	1.3 kg/m^3
ρ_w	Water density	1026 kg/m^3
C_{da}	Air drag coefficient	1.2×10^{-3}
C_{dw}	Water drag coefficient	5.5×10^{-3}
$P^{\star}$	Ice strength parameter	27.5×10^3 N/m^2
C	Ice concentration parameter	20
e	Ellipse ratio	2

Table 1: Physical parameters used in the VP sea ice model.

3. Numerical solvers

Time splitting methods are standard for solving the coupled sea ice system (2.2a)–(2.2c) [16], and in general, they are widely used to cope with the complex coupled system, e.g., in [4, 6, 16, 15]. The basic idea is to decouple the momentum equation (2.2a) from the transport equations and

solve it first, and then use the updated velocity to solve the transport equations, (2.2b) and (2.2c), together. The main difficulty here lies in the momentum equation due to the highly nonlinear feature of the viscous-plastic rheology.

To apply an explicit time-stepping scheme to the momentum equation, numerical stability dictates a time step on the order of 1 s for a 100 km grid resolution [10], or equivalently 1/100 s for a 10 km resolution grid, which is a typical spatial resolution for earth system models. Because of this very restrictive time step, it is recommended in [10] to use implicit time-stepping for the momentum equation. Implicit time-stepping requires the use of iterative methods which are notoriously difficult for nonlinear problems, however. To alleviate this issue, a Picard solver designed to repeatedly solve simple linear systems was proposed in [29]. Further investigation in [13] demonstrated the impractical slow convergence of the Picard solver which ultimately motivated the development of the JFNK solver in [11]. The JFNK solver is a nonlinear solver based on Newton's method [33]. It is a matrix-free approach in the sense that the Jacobian is utilized through matrix-vector products deduced from a first-order Taylor series expansion, and is useful since forming and storing the Jacobian matrix is prohibitively expensive [11]. The resulting linear system of equations is then in general solved by the preconditioned FGMRES method [34], which is a Krylov subspace method. Employing an inexact Newton method [35] can further improve robustness and computational efficiency. More details can be found in [36, 11, 37].

On the flip side, in order to entirely avoid implicit methods, the EVP model proposed by Hunke and Dukowicz [5] and then further modified by Hunke in [6], adds an artificial elastic term to the viscous-plastic constitutive equation, thereby relaxing the stability condition for an explicit time-stepping scheme. The basic idea of the EVP model is to approximate the VP solution by damping the resulting artificial elastic waves via subcycling [14].

Remark 3.1 (On the use of explicit time integration)**.** *Although using explicit time integration is non-standard for the VP model, and indeed is not realistic in the more general setting, it is well-suited for the purpose of this investigation. Specifically, studying the 1D VP model allows us to not be concerned about the cost in using explicit time stepping schemes, which in turn ensures that we do not conflate the errors that arise from using iterative solvers (namely stopping criteria) with the spatial discretization errors. We also avoid introducing new terms in the VP model, such as the EVP model does. In particular we are interested in avoiding the effects of numerical diffusion, which while serving to increase the underlying stability of the computation inevitably causes a reduction*

in accuracy. We emphasize that the spatial derivative operators employed in our analysis, namely WENO and CD, are regularly used in multi-dimensional environments, and that it is possible to couple with implicit time stepping algorithms. This investigation, therefore, is to demonstrate the potential use of higher order spatial derivative operators in sea ice modeling based on the numerical convergence properties we observe in our study of the 1D VP model. For completion we will compare our results to those obtained using the EVP model in Appendix A.

Before describing our approach to solving the 1D VP model in Section 4, we first take time to review the current methodology which we adapt to this simplified environment (as opposed to the 2D VP model). To this end, we will use a modified version of the JFNK solver, which we describe in Section 3.1 and hereafter refer to as the Newton solver. We also review the 1D EVP model in Section 3.2. We will compare the results using our new approach to those obtained using these current methodologies in Section 5.

3.1. The Newton solver

By limiting our study to the 1D VP model, we can accordingly simplify numerical implementation by directly using Newton's method instead of the JFNK solver, which would be required in more complex settings. Below we illustrate how this is implemented with a backward Euler (BE) time integration scheme for the momentum equation (2.2a).

The time-discretized 1D momentum equation is written as

$$\rho h^{n-1}\frac{u^n - u^{n-1}}{\Delta t} = \tau_a^n - \tau_w(u^n) + \frac{\partial \sigma(u^n, h^{n-1}, A^{n-1})}{\partial x}, \tag{3.1}$$

where the superscript n denotes the current time level. The numerical solution at the previous time level $n-1$ for (2.2) is known. Let $\mathbf{u}^n = \{u_j\}_{j=1}^N$ denote the approximation of u^n obtained by some finite difference spatial discretization technique at each grid point x_j, $j = 1, \dots N$.[2] The spatial discretization scheme will be specified on both non-staggered and staggered grids in Section 4. For now we generically define the solution on N grid points. At current time level n, we therefore seek a solution to

$$\mathbf{F}(\mathbf{u}^n) = \mathbf{0},$$

[2]To avoid cumbersome notation, for the rest of this paper we will use $\mathbf{u}$ to depict the vectorized solution of (2.2) (and not the continuous solution (2.1)).

where $\mathbf{F}(\mathbf{u}^n)$ is the difference between the right- and left-hand sides of (3.1) following spatial discretization.

Since we are focusing on a single time step, we can simplify the notation by dropping the superscript n, so that we seek the solution $\mathbf{u} = \mathbf{u}^n$. Using the velocity solution at the previous time level as the initial value $\mathbf{u}^{(0)}$, we iteratively solve a sequence of linearized systems to consecutively obtain $\mathbf{u}^{(1)}, \mathbf{u}^{(2)}, \cdots, \mathbf{u}^{(k)}, \cdots$ until some stopping criterion is satisfied. Algorithm 1 summarizes the iterative technique.

Algorithm 1 Newton solver

Start with an initial iterate $\mathbf{u}^{(0)}$ and calculate $\|\mathbf{F}(\mathbf{u}^{(0)})\|$, here $\|\cdot\|$ is the L2-norm.

for $k = 1$ to $k_{\max} = 150$ **do**

Solve $\mathbf{F}(\mathbf{u}^{(k-1)}) + \mathbf{J}(\mathbf{u}^{(k-1)})\delta\mathbf{u}^{(k)} = \mathbf{0}$ for $\delta\mathbf{u}^{(k)}$, where $\epsilon = 10^{-7}$ and $[\mathbf{J}(\mathbf{u}^{k-1})]_i := \dfrac{\mathbf{F}(\mathbf{u}^{(k-1)} + \epsilon\,\mathbf{e}_i) - \mathbf{F}(\mathbf{u}^{(k-1)})}{\epsilon}$, here $\mathbf{e}_i$ is the standard basis vector.

Set $\mathbf{u}^{(k)} = \mathbf{u}^{(k-1)} + \lambda\,\delta\mathbf{u}^{(k)}$, where $\lambda = \left[1, \frac{1}{2}, \frac{1}{4}, \frac{1}{8}\right]$ is successively reduced until $\|\mathbf{F}(\mathbf{u}^{(k)})\| < \|\mathbf{F}(\mathbf{u}^{(k-1)})\|$ or until $\lambda = \dfrac{1}{8}$.

Stop if $\|\mathbf{F}(\mathbf{u}^{(k)})\| < \gamma_{nl}\|\mathbf{F}(\mathbf{u}^0)\|$ with $\gamma_{nl} = 10^{-6}$.

end for

Remark 3.2 (Relationship between the Newton and JFNK solver)**.** *The solution obtained using Algorithm 1 is comparable to that obtained using the JFNK solver, which is commonly used in solving the 2D VP model. While the JFNK solver is generally more stable, using Newton's method will ensure that in our numerical tests we are appropriately comparing the spatial discretization error.*

3.2. The Elastic-Viscous-Plastic (EVP) model

In the EVP model, the velocity at time level n is obtained by *explicitly* solving the momentum equation from the previous time level $n-1$. In particular, the constitutive law was rewritten by Hunke and Dukowicz [5] to include a time dependence on the stress tensor. The velocity is then solved together with stress during subcycling. In the 1D case [32], the stress-strain relationship

$$\sigma = (\eta + \zeta)\frac{\partial u}{\partial x} - \frac{P}{2} \tag{3.2}$$

is equivalent to

$$\frac{\sigma}{\eta+\zeta}+\frac{P}{2(\eta+\zeta)}=\frac{\partial u}{\partial x}. \tag{3.3}$$

By adding an artificial elastic strain with an elastic parameter E, we obtain

$$\frac{1}{E}\frac{\partial \sigma}{\partial t}+\frac{\sigma}{\eta+\zeta}+\frac{P}{2(\eta+\zeta)}=\frac{\partial u}{\partial x}. \tag{3.4}$$

In the original version of the EVP model [5], the viscosities η and ζ were held fixed throughout the subcycling procedure. However, because the viscosities were not regularly updated, such linearization of the internal stress term caused the computed principal stress states to lie outside the elliptical yield curve [6]. To address this issue, Hunke [6] proposed to include the viscosities within the subcycling, while simultaneously changing the definition of the elastic parameter E to maintain the computational efficiency. Specifically, with E defined in terms of a damping timescale for elastic waves and T according to the equation $E=\dfrac{\zeta}{T}$, (3.4) can be rewritten as

$$\frac{\partial \sigma}{\partial t}+\frac{\sigma}{(1+e^{-2})T}+\frac{P}{2(1+e^{-2})T}=\frac{\zeta}{T}\frac{\partial u}{\partial x}. \tag{3.5}$$

The subcycling solution is advanced iteratively with subcycling time step Δt_e. This approach yields the time evolution of stress as a function of the velocity from the previous iterate according to

$$\frac{\sigma^s-\sigma^{s-1}}{\Delta t_e}+\frac{\sigma^s}{(1+e^{-2})T}+\frac{P^{n-1}}{2(1+e^{-2})T}=\frac{\zeta^{s-1}}{T}\frac{\partial u^{s-1}}{\partial x}, \tag{3.6}$$

where the subcycling iterate is denoted with the superscript s. With the newly calculated stress in (3.6), the velocity is subcycled according to

$$\rho h^{n-1}\frac{u^s-u^{s-1}}{\Delta t_e}=\tau_a^s-\tau_w^{s-1}+\frac{\partial \sigma^s}{\partial x}. \tag{3.7}$$

Observe that in the EVP model, the damping timescale T is a tuning parameter satisfying $\Delta t_e < T < \Delta t$, which is in general set to be $T=0.36\Delta t$ following the documentation of the CICE model [24]. In addition, we denote the number of subcycles by N_{sub}, satisfying $N_{sub}\times\Delta t_e=\Delta t$.

Remark 3.3. *We note that neither the JFNK solver nor the EVP model has entirely resolved the convergence issue. In particular, the JFNK solver is not robust, as it was demonstrated in [11] that the failure rate for the JFNK solver increases as the grid is refined. On the other hand, it was shown in [14] that the EVP approximate solution has notable differences from the reference solution, which becomes relatively more distinct with finer resolution. Furthermore, while both methods focus on the*

momentum equation, less attention is paid to the transport equations in the coupled system in either case. In particular, treating out-of-range issues for either the ice thickness or ice concentration is seldomly discussed. Hence it is possible to obtain unrealistic physical values for either or both when applying the solvers directly to the sea ice model. We therefore seek to address these issues in the 1D case so that we are better able to subsequently solve the more complicated 2D version in (2.1).

4. Proposed numerical methods

Motivated by the above discussion, in this section we propose an approach to help mitigate the limitations of existing solvers for both the VP and EVP sea ice models. We first discuss the WENO method [21] to advocate the use of higher-order methods for improving numerical accuracy and efficiency. We then describe the potential function method as a means to incorporate the physical restrictions of the ice thickness and concentration on top of the existing numerical methods. This will help to alleviate the out-of-range issues.

4.1. Weighted essentially non-oscillatory (WENO) scheme

A main goal of this investigation is to demonstrate the advantages of using higher-order methods to solve the sea ice model. We use the WENO method [21] as a prototype for two reasons. First, WENO is designed to have a higher-order convergence rate for smooth solutions than standard second-order three point stencil CD schemes, and second, WENO is able to maintain stable, non-oscillatory, and sharp discontinuity transitions so that it is suitable for sea ice with natural discontinuity feature of thickness and concentration. We verify that both of these properties hold in our numerical simulation of sea ice cover with and without sharp features.

Below we present the numerical implementation details of the WENO scheme [21], along with the other methods used to solve the momentum and transport equations (see Table 2). To keep our investigation self-contained, a brief description of the WENO scheme is provided in Appendix B. The second-order CD scheme is commonly used for spatial discretization of momentum equation [11, 16, 37] as well as transport equations [37]. A main purpose of this investigation is to analyze the numerical convergence properties for the 1D Hibler model and in particular to determine if either method is suitable.

We use the method of lines for time integration when employing either the WENO or CD spatial discretization scheme. In this regard, to ensure stability and maintain the accuracy obtained in the

equation type	scheme
momentum (2.2a)	WENO TVDRK3
	CD TVDRK3
transport (2.2b), (2.2c)	WENO TVDRK3
	CD TVDRK3
	Upwind

Table 2: Equations and corresponding solvers. The TVDRK3 scheme is provided in Algorithm 2. The WENO method is described in Appendix B. CD refers to the classical second-order three point stencil centered difference scheme, while upwind refers to the first-order two point one-sided finite difference method.

spatial derivative approximation, we use the third-order TVD Runge-Kutta (TVDRK3) method [38] for both the WENO and CD schemes. By employing the same time integration method (along with the same fixed time step) we ensure that we are comparing *only* the spatial discretization performances of WENO and CD – we are neither evaluating the time integration methods nor considering in our analysis the corresponding time integration error.

We furthermore compare these results to those obtained using CD with an implicit time integration (BE) and Newton solver for the momentum equation along with a first-order upwind scheme for the transport equations. Since the scheme with the (comparable) JFNK solver is common in practice, [11, 16], we will refer to this particular combination as the "reference scheme" from now on. For completion we describe the numerical implementation of the upwind scheme for the transport equations (see (4.2) in Section 4.1.2). Our numerical examples in Section 5.3 and Section 5.4 provide case studies for the mixed time integration approach. Finally we note that it is of course possible to use a different spatial discretization for each equation in the system. As we did not observe any advantage in this (more complex) approach, we do not include these results here.

4.1.1. The momentum equation

To solve the momentum equation by the WENO scheme, we use higher-order finite differencing for (2.2a), following [39] for nonlinear degenerate parabolic equations. In particular, $\frac{\partial u}{\partial x}$ and $\frac{\partial \sigma}{\partial x}$ are discretized using the fifth-order finite difference WENO method for conservation laws [40] based on the left-biased stencil and right-biased stencil, respectively.

We consider both periodic and Dirichlet boundary conditions. Periodic boundary conditions

allow us to avoid errors introduced by numerical extrapolation at the boundaries. That said, the complexities introduced at the boundaries here are not fundamentally different from other PDE models. Here we construct a non-staggered grid so that all variables are defined at the center of each grid cell. That is, we seek the solution at the $j = 1, \ldots, N$ midpoints of each cell, $x_{j-\frac{1}{2}} = x_j - \frac{1}{2}\Delta x$, with $x_j = j\Delta x$ and $\Delta x = \frac{L}{N}$ where L is the domain length. For periodic boundary conditions, the "ghost" point values outside the computational domain are naturally obtained from the periodicity assumption. For a more physically realistic scenario, we consider an ocean-land boundary in which case homogeneous Dirichlet boundary conditions ($u = 0$) are applied at either end of the model domain. To incorporate the prescribed boundary conditions accurately, we construct a non-staggered grid where all the variables are defined on vertices $\{x_j\}_{j=0}^N$. The ghost point values are simply chosen to be the same as the values of their closest neighbors within the computational domain. That is, for a generic variable z, we take

$$z_j = \begin{cases} z_0 & \text{if} \quad j < 0; \\ z_N & \text{if} \quad j > N. \end{cases} \tag{4.1}$$

On the other hand, for the commonly used CD scheme, we follow [11, 16, 37] and construct a 1D version of the staggered Arakawa C-grid [41], where the velocity u is defined on vertices $\{u_j\}_{j=0}^N$, and the traces h and A are defined at the center of each grid cell, $\{h_{j-\frac{1}{2}}\}_{j=1}^N$ and $\{A_{j-\frac{1}{2}}\}_{j=1}^N$ respectively. Correspondingly, the stress σ, the viscosities η and ζ and the ice strength P are also defined at the center of each grid cell. To solve for the velocity u in the momentum equation (2.2a), we take $h_j = \frac{1}{2}(h_{j+\frac{1}{2}} + h_{j-\frac{1}{2}})$ for $j = 1, \cdots, N-1$. We then approximate $\frac{\partial u}{\partial x}$ at each cell center as

$$\{du\}_{j-\frac{1}{2}} = \frac{u_j - u_{j-1}}{\Delta x},$$

so that $\sigma = (\eta + \zeta)\frac{\partial u}{\partial x} - \frac{P}{2}$ is defined at $x_{j-\frac{1}{2}}$. This leads to the approximation $\frac{\partial \sigma}{\partial x}$ at each vertex given by

$$\{d\sigma\}_j = \frac{\sigma_{j+\frac{1}{2}} - \sigma_{j-\frac{1}{2}}}{\Delta x}.$$

The scheme is then complemented with either periodic boundary conditions or homogeneous Dirichlet boundary conditions as discussed above.

4.1.2. The transport equations

Similarly to the momentum equation, the fifth-order WENO method for conservation laws [40] is also used to solve the transport equations (2.2b) and (2.2c) with either periodic or Dirichlet

boundary conditions. In the latter case, suitable ghost point values for numerical flux $\widehat{f}$ need to be prescribed on both sides of the domain. When the boundary point corresponds to $\widehat{f}' \geq 0$, the ghost point values are taken to be 0. On the other hand when the boundary point corresponds to $\widehat{f}' \leq 0$, we use linear extrapolation resulting in[3]

$$\widehat{f}_j = \begin{cases} 2\widehat{f}_0 - \widehat{f}_{-j} & \text{if} \quad j < 0; \\ 2\widehat{f}_N - \widehat{f}_{2N-j} & \text{if} \quad j > N. \end{cases}$$

Both the second-order CD scheme [37] and the first-order upwind scheme [11, 14, 16] have been frequently used to solve the transport equations, where the staggered grid is adopted for spatial discretization of the variables as explained in Section 4.1.1. In the CD scheme, using a similar strategy to discretize the transport equation (2.2b) for h as was done for the momentum equation (2.2a), we approximate $\dfrac{\partial}{\partial x}(uh)$ at each cell center as

$$\{d(uh)\}_{j-\frac{1}{2}} = \frac{(uh)_j - (uh)_{j-1}}{\Delta x}.$$

We similarly solve A using the same spatial discretization for the transport equation (2.2c). To numerically impose the homogeneous Dirichlet boundary conditions we apply $u_0 = 0$ (similarly $u_N = 0$) so that

$$(uh)_0 = u_0 h_0 = 0,$$

leading to

$$\{d(uh)\}_{\frac{1}{2}} = \frac{(uh)_1 - (uh)_0}{\Delta x} = \frac{(uh)_1}{\Delta x}$$

for the transport equation (2.2b) (similarly for $\{d(uh)\}_{N-\frac{1}{2}}$). The Dirichlet boundary conditions also yield analogous equations for A at the boundaries in (2.2c). On the other hand, the first-order upwind scheme for the transport equation (2.2b) of h is given by

$$\frac{h^n_{j-\frac{1}{2}} - h^{n-1}_{j-\frac{1}{2}}}{\Delta t} + \frac{(uh)^{n-1}_{j-\frac{1}{2}} - (uh)^{n-1}_{j-\frac{3}{2}}}{\Delta x} = 0 \qquad \text{for} \quad u^{n-1}_{j-\frac{1}{2}} > 0, \tag{4.2a}$$

$$\frac{h^n_{j-\frac{1}{2}} - h^{n-1}_{j-\frac{1}{2}}}{\Delta t} + \frac{(uh)^{n-1}_{j+\frac{1}{2}} - (uh)^{n-1}_{j-\frac{1}{2}}}{\Delta x} = 0 \qquad \text{for} \quad u^{n-1}_{j-\frac{1}{2}} < 0, \tag{4.2b}$$

[3]This type of boundary condition is referred to as anti-symmetric in [20]. A more general and detailed discussion on WENO scheme boundary conditions can be found there.

for $j = 2, \cdots, N-1$, where because of the staggered grid we compute $u_{j-\frac{1}{2}} = \dfrac{1}{2}(u_{j-1} + u_j)$. To incorporate the homogeneous Dirichlet boundary condition $u_0 = 0$ (similarly $u_N = 0$), we update $h_{\frac{1}{2}}$ with the modified scheme

$$\frac{h^n_{\frac{1}{2}} - h^{n-1}_{\frac{1}{2}}}{\Delta t} + \frac{(uh)^{n-1}_{\frac{1}{2}} - (uh)^{n-1}_0}{\frac{1}{2}\Delta x} = 0 \qquad \text{for} \quad u^{n-1}_{\frac{1}{2}} > 0, \tag{4.3a}$$

$$\frac{h^n_{\frac{1}{2}} - h^{n-1}_{\frac{1}{2}}}{\Delta t} + \frac{(uh)^{n-1}_{\frac{3}{2}} - (uh)^{n-1}_{\frac{1}{2}}}{\Delta x} = 0 \qquad \text{for} \quad u^{n-1}_{\frac{1}{2}} < 0, \tag{4.3b}$$

and make use of

$$(uh)_0 = u_0 h_0 = 0.$$

The transport equation (2.2c) of A is solved similarly.

Finally, we discuss the time integration technique TVDRK3, which is necessary to maintain stability when employing both WENO and CD spatial discretization schemes. We consider the ordinary differential equation

$$\frac{dz}{dt} = L(z),$$

for a generic variable z, where $L(z)$ is a discretization of the spatial operator. The TVDRK3 method advances the solution at the current time level, z^{n-1}, to the solution at the next time level, z^n, according to Algorithm 2. The value z^0 corresponds to the initial conditions.

Algorithm 2 TVDRK3 time integration method for a single time step

INPUT: z^{n-1} and $L(z^{n-1})$

OUTPUT: The solution z^n at time level n.

$z^{(1)} = z^{n-1} + \Delta t\, L(z^{n-1})$,

$z^{(2)} = \frac{3}{4} z^{n-1} + \frac{1}{4} z^{(1)} + \frac{1}{4}\Delta t\, L(z^{(1)})$,

$z^n = \frac{1}{3} z^{n-1} + \frac{2}{3} z^{(2)} + \frac{2}{3}\Delta t\, L(z^{(2)})$.

4.2. Potential function method

Due to its physical interpretation, the variable ice thickness h in the sea ice model must remain non-negative. Similarly, the ice concentration value A must be between 0 and 1. It is crucial for the numerical methods to preserve both of these properties to ensure that a meaningful solution is

obtained. Motivated by the double-well potential function in the phase field method [27, 28], where the resulting equation is limited to a particular set of prescribed values due to the local minima of the potential function, we develop the potential function method here to impose the corresponding restrictions of ice thickness and ice concentration.

We begin by illustrating the potential function method on the transport equation of ice concentration A in (2.2c) and note that the case for ice thickness h in (2.2b) similarly follows. First, to restrict ice concentration A so that $0 \leq A \leq 1$, we define a potential function in a piecewise manner as

$$f(A) = \begin{cases} \gamma_1 f_1(A), & \text{if} \quad A < 0, \\ 0, & \text{if} \quad 0 \leq A \leq 1, \\ \gamma_2 f_2(A), & \text{if} \quad A > 1, \end{cases} \tag{4.4}$$

where $f_1 > 0$ and $f_2 > 0$ for all A, and $\gamma_1 > 0$ and $\gamma_2 > 0$ are parameters chosen so that f has minima on $[0, 1]$. For example, if both f_1 and f_2 are linear functions, a particular form of f might be

$$f(A) = \begin{cases} -\gamma_1 A, & \text{if} \quad A < 0, \\ 0, & \text{if} \quad 0 \leq A \leq 1, \\ \gamma_2 (A-1), & \text{if} \quad A > 1. \end{cases} \tag{4.5}$$

The transport equation (2.2c) is then modified by adding a forcing term given by the gradient of the potential. This has the effect of the ice concentration experiencing a gradient force that tracks down to the physical range $[0, 1]$. The resulting equation is given by

$$\frac{\partial A}{\partial t} + \frac{\partial}{\partial x}(u\, A) = -f'(A). \tag{4.6}$$

Observe that for the piecewise linear case, the forcing term $-f'(A)$ is piecewise constant, meaning that the force transition is not continuous. To enable a more desirable smooth transition for this term we will instead choose both f_1 and f_2 to be quadratic and define f as

$$f(A) = \begin{cases} \gamma_1 A^2, & \text{if} \quad A < 0, \\ 0, & \text{if} \quad 0 \leq A \leq 1, \\ \gamma_2 (A-1)^2, & \text{if} \quad A > 1. \end{cases} \tag{4.7}$$

The corresponding forcing term is now given by

$$f'(A) = \begin{cases} 2\gamma_1 A, & \text{if} \quad A < 0, \\ 0, & \text{if} \quad 0 \leq A \leq 1, \\ 2\gamma_2 (A-1), & \text{if} \quad A > 1, \end{cases} \tag{4.8}$$

which is clearly continuous.

4.2.1. Determining parameters γ_1 and γ_2

We now must determine parameters γ_1 and γ_2 in (4.5) to ensure that A stays in range, $0 \leq A \leq 1$. To this end, we first prescribe a Lagrangian representation of the ice concentration field A, denoted as

$$B(t) = A(x(t), t),$$

which allows us to express the ice concentration field as a function of time t only. From the method of characteristics we have $\dot{x} = \dfrac{dx}{dt} = u(x,t)$, so that the modified transport equation (4.6) can be written as

$$\dot{B} = -f'(B) - B\,\frac{\partial u}{\partial x}.$$

Using local analysis around $B = 0$ and $B = 1$ to respectively determine the appropriate ranges for γ_1 and γ_2, we conduct linear approximation to u and estimate $\dfrac{\partial u}{\partial x}$ as $a = a(x)$. This leads to the ODE given by

$$\dot{B} = -f'(B) - aB. \tag{4.9}$$

Determining a range for γ_1: To determine an appropriate range for γ_1, we use local analysis around $B = 0$ so that (4.9) becomes

$$\dot{B} = -2\gamma_1 B - aB, \qquad B(0) = B_0, \tag{4.10}$$

which has the analytical solution

$$B = B_0 e^{-(2\gamma_1 + a)t}. \tag{4.11}$$

285 The out-of-range case we are considering is for the case where the numerical solution yields the non-physical *negative* ice concentration. It therefore follows that $B_0 < 0$, and from this observation we define the "out-of-range" error $\delta_1 := -B_0$. Our goal then is to "nudge" the numerical solution so that it moves back into range. Accordingly, we need B to be an increasing function, or equivalently

$\dot{B} > 0$ in (4.10). Clearly this requires $\gamma_1 > -\frac{a}{2}$. Observe from (4.11) that it is always true that $B < 0$, so the ice concentration will never fall out of range near the value 1 as long as $\gamma_1 > -\frac{a}{2}$.

Imposing this constraint is straightforward. Since A is initially within $[0, 1]$ for the whole domain and $f'(A) = 0$ everywhere, we start by solving the non-modified transport equation (2.2c). Now suppose that at some later time there is a point in the domain for which the numerical scheme computes $A < 0$. This is equivalent to $B_0 < 0$ in (4.10), establishing the need to modify the transport equation by adding an extra forcing term $-f'(A) = -2\gamma_1 A$ from (4.8).

The analysis with respect to (4.11) applies only to constructing a lower bound for γ_1, as indeed choosing γ_1 too large would dramatically affect the behavior of (4.6), creating a greater discrepancy from the original problem (2.2c), and possibly leading to non-physical oscillatory behavior over time. We can avoid this problem altogether by using a surrogate one-step forward Euler approximation of (4.10) given by

$$B = -(2\gamma_1 + a)B_0\Delta t + B_0, \tag{4.12}$$

which simplifies both the analysis and numerical implementation for determining the bounds of γ_1. Specifically, based on the arguments above requiring B to be an increasing function, we still need $\gamma_1 > -\frac{a}{2}$. On the other hand, we also need $B \leq 1$ to ensure that A stays within $[0, 1]$. As per the discussion above, the legitimacy of (4.6) requires $B > 0$ to remain close to 0, that is $B \leq \widehat{\delta}_1$ for some small number $\widehat{\delta}_1 > 0$. Substituting these conditions into (4.12) we obtain

$$\gamma_1 \leq -\frac{a}{2} + \frac{\widehat{\delta}_1/\delta_1 + 1}{2\Delta t},$$

yielding the finite range for γ_1 as

$$-\frac{a}{2} < \gamma_1 \leq -\frac{a}{2} + \frac{\widehat{\delta}_1/\delta_1 + 1}{2\Delta t}. \tag{4.13}$$

Remark 4.1. *Recall that δ_1 measures the discrepancy between negative A and 0, while $\widehat{\delta}_1$ measures the amount the numerical solution is "nudged" back into range. Since both values are small, we see from* (4.13) *that the range of admissible γ_1 is proportional to $\frac{1}{\Delta t}$, which also provides insight on the choice of γ_1. We further note that since a is the linear approximation of $\frac{\partial u}{\partial x}$ (see discussion surrounding* (4.9)*), $|a|$ can be reasonably assumed to be less than 1 s^{-1}, due to the fact that $|u|$ is generally less than 1 m/s and thus the discretized value $|\Delta u|$ is much smaller than the order (km) of the spatial resolution Δx. It follows that to maintain consistency between* (4.6) *and* (2.2c) *it is*

desirable to choose γ_1 close to $-\frac{a}{2}$. Finally, we point out that since a can be estimated in early simulations (before A goes out of range) and Δt is a user-defined parameter, choosing γ_1 can be somewhat automated.

It is important to point out the trade-off between ensuring that A stays within range and conservation. That is, applying (4.6) (or any type of post-processing) will cause some conservation discrepancy, and this increases with γ_1. By contrast, when γ_1 is closer to the lower bound, there is less conservation discrepancy, but in this case using the potential function method may not be effective in keeping A within its physically meaningful range. More details will be provided in Section 5.3.

Determining a range for γ_2:

Using a similar approach, we now consider the local analysis around $B = 1$, corresponding to the case where A goes out of range near the value 1. The ODE in (4.9) around $B = 1$ reduces to

$$\dot{B} = -2\gamma_2(B-1) - aB, \qquad B(0) = B_0, \tag{4.14}$$

which yields the analytical solution

$$B = (B_0 - \frac{2\gamma_2}{2\gamma_2 + a})e^{-(2\gamma_2+a)t} + \frac{2\gamma_2}{2\gamma_2 + a}. \tag{4.15}$$

Since we are now considering the out-of-range solution $A > 1$, we have $B_0 = 1 + \delta_2$, where $\delta_2 = |1 - B_0| > 0$ is again the magnitude of the out-of-range error. In this case we seek γ_2 so that B is decreasing, or equivalently $\dot{B} < 0$, which wil "nudge" the numerical solution so that A gets back in range of possible physical solutions, $[0, 1]$. Clearly, then, $\gamma_2 > -\frac{aB_0}{2(B_0-1)} = \frac{a(1+\delta_2)}{2\delta_2}$. We must also ensure that $B \geq 0$ for all $t \geq 0$ so that we don't fall out of range on the left side of the solution interval. To this end, we first observe that (4.15) can also be written as

$$B = (B_0 - 1)e^{-(2\gamma_2+a)t} + \frac{a}{2\gamma_2 + a}(e^{-(2\gamma_2+a)t} - 1) + 1, \tag{4.16}$$

from which it is immediately apparent that $B > 1$ for all γ_2 as long as $a \leq 0$. It is also possible to show that $B \geq 0$ for $a \leq 1$. From the discussion within Remark 4.1 we can assume $|a| < 1$ s^{-1}, so that $B \geq 0$ holds for all γ_2 in the given problem.

As was done in (4.12), we can again consider the one-step forward Euler approximation

$$B = -(2\gamma_2 + a)B_0\Delta t + 2\gamma_2\Delta t + B_0. \tag{4.17}$$

The requirements of B decreasing with $B \geq 1 - \widehat{\delta}_2$ lead to the range of γ_2 given by

$$\frac{a(1+\delta_2)}{2\delta_2} < \gamma_2 \leq \frac{a(1+\delta_2)}{2\delta_2} + \frac{\widehat{\delta}_2/\delta_2 + 1}{2\Delta t}. \tag{4.18}$$

As before, we add the extra forcing term, in this case $-f'(A) = -2\gamma_2(A-1)$, whenever $A > 1$ results from the numerical solver. Finally, we also note that the same procedure is implemented for the ice thickness h when the numerical solver causes it to become negative. As we will see in Section 5, our integrated method, which combines the WENO TVDRK3 scheme with the potential function approach, yields an accurate and stable numerical solver for the 1D Hibler model.

5. Numerical experiments

We provide four numerical experiments to illustrate the behavior of our proposed methods for the 1D sea ice simulation model. The first experiment is to corroborate the higher rate of convergence for WENO as compared to CD for smooth solutions. The capacity to resolve discontinuities (sharp features) in the sea ice covers is verified in the second test, while the third example shows how the potential function is implemented in situations where the numerical solutions A and h fall out of range. Finally, we illustrate the benefits of integrating our proposed methods by comparing the WENO TVDRK3 potential function numerical solver to the reference scheme (see discussion preceding Section 4.1.1) that uses a "cut-off" post-processor to keep h and A within physical range on the transport equations.

5.1. Numerical convergence analysis

To assess the convergence rate of WENO, we consider a test problem in a domain $\Omega = [0,\ 2000]$ km with a known analytical solution. This is, of course, generally not the case as the sea ice model has no known solutions. We construct the proposed solutions so that their values are consistent in magnitude to their corresponding true physical values:

$$\begin{aligned} u_{\text{true}} &= (\sin(2\pi x/(2\times 10^6) + 5t/518400 - \pi/2) + 1) \times 0.001 + 0.2, \\ h_{\text{true}} &= (\sin(2\pi x/(2\times 10^6) + 5t/518400 - \pi/2) + 1) + 0.1, \\ A_{\text{true}} &= (\sin(2\pi x/(2\times 10^6) + 5t/518400 - \pi/2) + 1) \times 0.15 + 0.7. \end{aligned} \tag{5.1}$$

We then construct our test cases by adding appropriate extra forcing terms to the governing equations. This is done by introducing to the right hand side of each equation in (2.2) the forcing terms

which are obtained by plugging into the left hand side terms corresponding to the constructed solutions, so that our test system of equations becomes

$$\rho h\frac{\partial u}{\partial t} - \tau_a + \tau_w(u) - \frac{\partial \sigma}{\partial x}(u) = \rho h_{\text{true}}\frac{\partial u_{\text{true}}}{\partial t} - \tau_a + \tau_w(u_{\text{true}}) - \frac{\partial \sigma}{\partial x}(u_{\text{true}}), \tag{5.2a}$$

$$\frac{\partial h}{\partial t} + \frac{\partial}{\partial x}(u\,h) = \frac{\partial h_{\text{true}}}{\partial t} + \frac{\partial}{\partial x}(u_{\text{true}}\,h_{\text{true}}). \tag{5.2b}$$

$$\frac{\partial A}{\partial t} + \frac{\partial}{\partial x}(u\,A) = \frac{\partial A_{\text{true}}}{\partial t} + \frac{\partial}{\partial x}(u_{\text{true}}\,A_{\text{true}}). \tag{5.2c}$$

In (5.2a) we emphasize that τ_w and $\dfrac{\partial \sigma}{\partial x}$ are both functions of u (see (2.4) and (2.5)). Conversely τ_a (see (2.3)) cancels out since it does not depends on u, h, or A, implying that the surface wind u_a does affect the convergence results. Initial conditions for the system are obtained by plugging $t = 0$ into (5.2).

The total simulation time is $T = 5$ s. The time step $\Delta t = 10^{-4}$ s is intentionally chosen to be small enough to ensure that the time discretization error does not affect the spatial convergence rates. It furthermore allows us to conduct convergence tests directly on the VP sea ice model for both the WENO and CD explicit spatial discretization schemes without the usual concern for the stability issue associated with explicit methods.

Table 3 compares the relative ℓ_2 errors for increasing resolutions with each spatial discretization choice. We observe second-order convergence for all three variables for the CD case, which is consistent with the standard convergence analysis results for CD schemes. By employing the WENO scheme in the ideal case, one would expect to obtain sixth-order convergence for the velocity u and fifth-order convergence for both the ice thickness h and ice concentration A. However, due to the complexity and non-linearity of the sea ice model, coupled with the fact that the added extra forcing terms are not being updated in the stages of TVDRK3 time integration, theoretical accuracy is unlikely to be obtained. We still observe higher-order convergence for all three variables as compared to the CD results. In addition, a direct comparison of the error magnitudes for all three variables indicates that the WENO scheme indeed provides more accurate results than those obtained using CD, noting that WENO appears to be mainly affected by round-off error at 10 km resolution.

5.2. A simulation of sea ice with sharp features

In this example we test the performance of the WENO scheme on a simulation of a sea ice cover with sharp features. To better capture the solution behavior near the discontinuity region while

CD TVDRK3						
resolution Δx	u error	u rate	h error	h rate	A error	A rate
40 km	2.6655e-06		4.4967e-09		1.0362e-09	
20 km	6.6698e-07	1.9987	1.1247e-09	1.9992	2.5920e-10	1.9991
10 km	1.6692e-07	1.9984	2.8120e-10	1.9998	6.4883e-11	1.9981

WENO TVDRK3						
resolution Δx	u error	u rate	h error	h rate	A error	A rate
40 km	5.2407e-07		1.3483e-11		8.8200e-12	
20 km	2.1769e-08	4.5894	5.8573e-13	4.5248	9.2062e-13	3.2601
10 km	8.3211e-10	4.7093	8.8497e-14	2.7265	5.5688e-13	0.7252

Table 3: A comparison of CD and WENO spatial discretization errors for increasing resolution.

maintaining periodic boundary conditions, the structure of ice is designed such that relatively solid ice covers both ends of the domain and a very thin layer of ice is in the center of the domain. This is realized via a discontinuous setting on the initial conditions of ice thickness and concentration given by

$$
\begin{aligned}
u &= 0 \text{ m/s} \quad \text{on} \quad [0, 2000] \text{ km}, \\
h &= \begin{cases} 0.01 \text{ m} \quad \text{on} \quad [400, 1600] \text{ km}, \\ 2 \text{ m} \quad \text{on} \quad [0, 400] \cup [1600, 2000] \text{ km}, \end{cases} \\
A &= \begin{cases} 0.01 \quad \text{on} \quad [400, 1600] \text{ km}, \\ 0.8 \quad \text{on} \quad [0, 400] \cup [1600, 2000] \text{ km}. \end{cases}
\end{aligned} \tag{5.3}
$$

For the external forcing in (2.3) we impose uniform constant wind forcing $u_a = 10$ m/s.

Remark 5.1. *As the WENO and CD schemes yield theoretically different convergence rates, for a direct comparison, we also consider the so-called* linear WENO scheme*, [40], for which the nonlinear weights are replaced by linear ones of the same order accuracy. Note that this is equivalent to using a fifth-order upstream centered scheme (upstream in time, centered in space). Due to the combined stencil, the highest possible order of accuracy is obtained in smooth regions. The results are oscillatory near discontinuities, however.*

Our results are displayed for the VP model in (2.2).[4] The simulation is run with a spatial resolution of $\Delta x = 10$ km and time step $\Delta t = 1$ s for a total simulation time of 1 hour (3600 s). Figure 1 compares the results using WENO (top row), linear WENO (middle row), and CD (bottom row) spatial discretizations for the simulation of the sea ice model with sharp features as constructed using the initial conditions given in (5.3). Observe that the solutions for each variable u (left column), h (middle column) and A (right column) are discontinuous. The solution plots demonstrate that only WENO maintains a sharp non-oscillatory solution for the velocity u in each sub-region, with a sharp overshoot occurring in the CD velocity profile. We also note that while the WENO solution is plotted at the final time of 1 hour, the solutions for the linear WENO and CD are presented at 2000 s and at 2331 s, respectively, since the oscillations eventually cause these solutions to blow up. There is less distinction between the methods in the ice thickness and ice concentration solutions, which all retain the initial profiles while moving slightly toward the ends of the domain due to the exerted wind forcing. However, since they are coupled with velocity, the CD and linear WENO solutions will also blow up before the final time.

The simulation results lead us to conclude that while we are able to properly resolve the discontinuities and obtain a stable solution using WENO, this cannot be accomplished using either the CD or the traditional higher-order (linear WENO) schemes.

Remark 5.2. *We also run this numerical experiment using the reference scheme (see paragraph above Section 4.1.1) with a spatial resolution of* $\Delta x = 10$ *km and time step* $\Delta t = 180$ *s for a total simulation time of 1 hour (3600 s). The solution plots at the 3060 s are presented in Figure 2. Although the solutions do not blow up, oscillations are apparent in the velocity profile between 1600 km and 2000 km of the domain. Indeed, the Newton solver fails 15 out of 20 times. At earlier times (results not shown here), one could observe that the oscillations in the velocity profile stem from the discontinuity point at 1600 km, and is due to the CD scheme not being able to resolve the discontinuities. This example further demonstrates that the computed solutions are unreliable whenever the Newton solver fails. While stability may be enhanced via the use of implicit time integration schemes and/or low order methods, it is important to emphasize that this does not mean that we obtain an* accurate *solution. In particular, we can obtain a "wrong" solution without numerical blow up. Fundamentally, this is why both stability and accuracy are needed to obtain*

[4] Similar results are obtained for the EVP solver model and are presented in Appendix A.

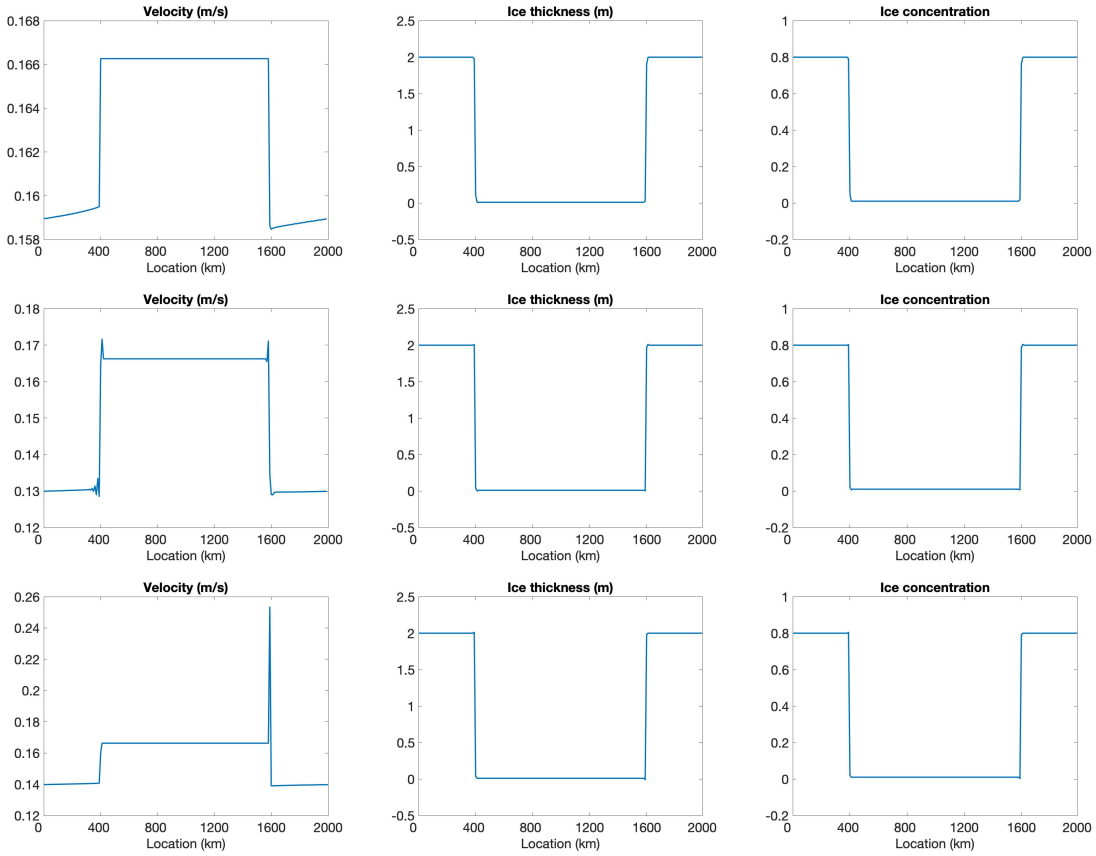

Figure 1: Simulation of sea ice with sharp features. (Top) solution plots using WENO at 1 hour; (middle row) solution plots using linear WENO at 2000 s; (bottom) solution plots using CD at 2331 s. (Left) velocity u; (middle column) ice thickness h; (right) ice concentration A.

numerical convergence.

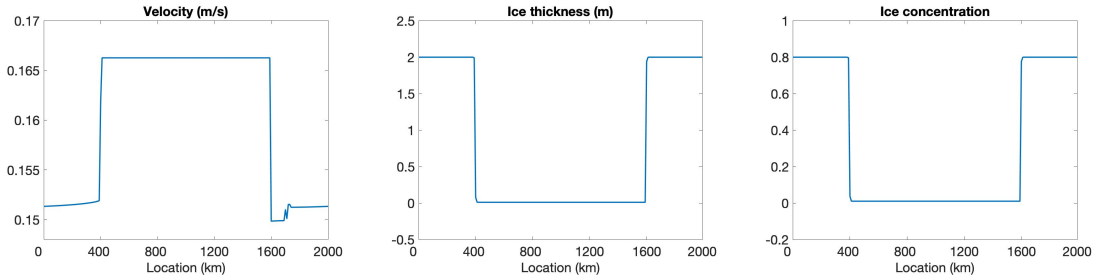

Figure 2: Simulation of the sea ice with sharp features. The solution plots are constructed using the reference scheme at 3060 s . (Left) velocity u; (middle) ice thickness h; (right) ice concentration A.

5.3. Incorporating the potential function method into the solver

We now test the model for which no exact solution is known. The main goal of this numerical test is to determine how out-of-range issues, namely $A < 0$, $A > 1$, or $h < 0$, may be effectively mitigated using the potential method described in Section 4.2.

We use BE time integration with CD spatial discretization and Newton solver to solve the momentum equation, along with TVDRK3 with CD scheme for transport equations. We note that in choosing to use an implicit time-stepping method for solving (2.2a) we avoid issues concerning stability. Moreover, with regard to the transport problem, we note that the WENO scheme does not yield out-of-range negative solutions for either A or h. Hence to determine the efficacy of the potential method we apply the CD scheme (using explicit time-stepping) to the transport equations (2.2b) and (2.2c). As discussed in 4.1, we also use the 1D version of the staggered Arakawa C-grid [41].

We run all the experiments on a domain of length 2000 km for a total integration time of 6 days. We choose a spatial resolution of 20 km and 90 s as the time step. The initial conditions are constant throughout $[0, 2000]$ km and given by

$$u(x,0) = 0 \text{ m/s}, \quad h(x,0) = 1 \text{ m}, \quad A(x,0) = 0.9.$$

We impose Dirichlet boundary conditions so that

$$u(0,t) = u(2000,t) = 0 \text{ m/s}. \tag{5.4}$$

Observe that since the ocean is considered to be at rest in this model, the only variable external forcing term is the wind, which is imposed uniformly as a constant given by

$$u_a(x,t) = 10 \text{ m/s}.$$

For comparison purposes we first run the simulation without applying the potential function method. Throughout the 6-day simulation, we find that the largest A value is 1.0540, the smallest A value is -0.1445, and the smallest h value is -0.1606, which are all out of range.

To employ the potential function method, we first simulate the model (without incorporating the potential function method into the transport equations) until the time T_1 for which $\min_x\{A(x,T_1)\} < 0$.[5] The potential function variables corresponding to (4.10) are then determined as

$$a \approx \frac{\partial u}{\partial x}, \quad B_0 = A.$$

While B_0 is determined directly from the numerical implementation of the scheme, as previously mentioned after (4.9), a is computed as a linear approximation of $\dfrac{\partial u}{\partial x}$. Following the discussion in Section 4.2, we then find a uniform bound for γ_1 by computing

$$\gamma_{1,\min} = \max_x \Big\{ -\frac{a}{2} \Big\}, \qquad \gamma_{1,\max} = \min_x \Big\{ -\frac{a}{2} + \frac{\widehat{\delta}_1/\delta_1 + 1}{2\Delta t} \Big\},$$

where $\delta_1 = -B_0$ and we assume $\widehat{\delta}_1 = \delta_1$ for simplicity. The process is similar for determining γ_2 for when $\max_x\{A(x,T_2)\} > 1$, $T_2 > 0$ and choosing $\widehat{\delta}_2 = \delta_2$, and in our experiment we obtain

$$\gamma_1 \in (3.6682 \times 10^{-7},\ 0.0111), \qquad \gamma_2 \in (0.0075,\ 0.0186).$$

Finally, similarly derived as for γ_1 and γ_2, the corresponding range for the parameter γ associated with $h < 0$ is

$$\gamma \in (3.6682 \times 10^{-7},\ 0.0111). \tag{5.5}$$

Based on these results and the discussion in Section 4.2, we choose

$$\gamma_1 = 10^{-3}, \qquad \gamma_2 = 10^{-2}, \quad \text{and} \quad \gamma = 10^{-3}.$$

These parameter choices will be discussed further in Remark 5.4. We then run the remainder of the
410 simulation, up until final time $T = 6$ days, with the potential function method now incorporated into the transport equations. For comparison, we also run the simulation using a "cut-off" post-processor, which simply removes any value outside the desired range.

The solutions of u, h, and A are displayed in Figure 3, where the top row depicts the solutions without employing the potential function method or the cut-off post-processor, the second row

[5] We only do this process one time for each out-of-range situation, $A < 0$, $A > 1$, and $h < 0$. The potential function parameters then remain fixed for all time.

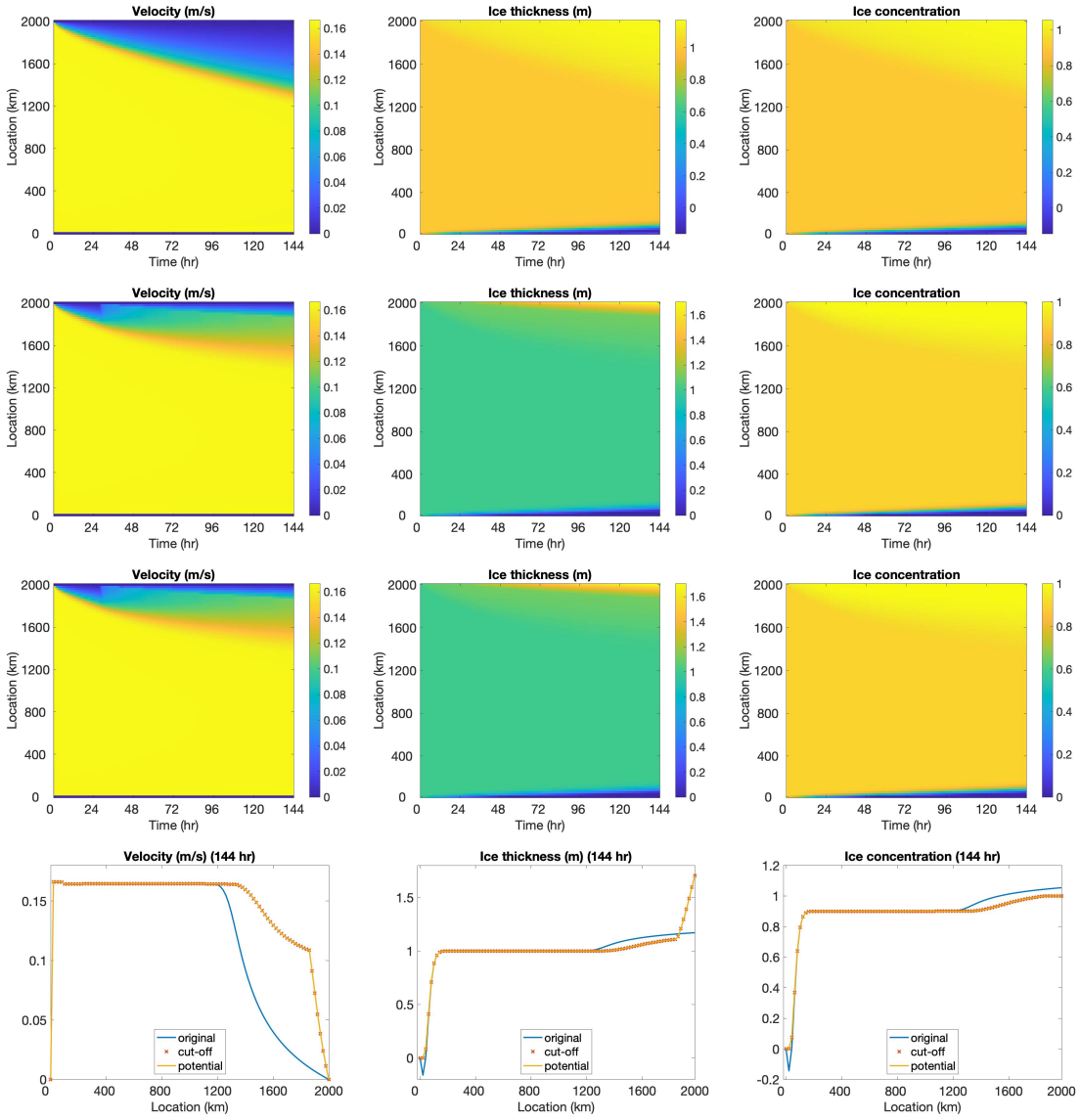

Figure 3: Potential function method example. (Top) images of computed solutions without applying the potential function method or the cut-off post-processor; (second row) images of computed solutions applying potential function method; (third row) images of computed solutions applying the cut-off post-processor; (bottom) solutions plots at final time.

shows the solutions when the potential function is used, the third row shows the solutions using the cut-off post-processor, and the bottom row shows the solution plots at the final time. It is evident that using the potential function yields some differences in the solution. The change of color shade in the velocity image around the 2000 km boundary of the region at roughly 30 hours indicates the situation when the non-physical values are detected and potential function starts to take effect. With the potential function method, the velocity remains a relatively large value on a larger portion of the domain and decreases to 0 in a sharper manner towards the end of the boundary. The behavior of the ice thickness near the boundary, especially around 2000 km, dramatically changes due to the application of the potential function method. In particular, the non-physical negative values near the left boundary are replaced by smoother physically meaningful values. Also, the thickness value is much larger near the right boundary, and the ridging effect is more clearly observed. This makes more sense physically for ridging on the ocean-land boundary. For the ice concentration, non-physical negative values near the left boundary and non-physical large values near the right boundary are also appropriately treated by the potential function method. Finally, Figure 3 (bottom) shows similar behavior when either the potential function method or the cut-off post-processor is employed to reduce out of range issues. Here "original" refers to the numerical scheme without employing either the potential function method or the cut-off post-processor. A couple of remarks are in order.

Remark 5.3. *The numerical tests demonstrate that the potential function method plays an important role in preserving the bounds for ice thickness and ice concentration in the sea ice model. It has the advantage of not requiring any post-processing, which may introduce discontinuities into the solution profile, a problem that can become more apparent in more realistic environments, where the true solution exhibits more fluctuating behavior. In future work we will investigate how the potential function method performs in more complicated scenarios, such as in the case of non-uniform wind forcing or in higher-dimensional settings.*

Remark 5.4. *As already discussed, the parameters in the potential function are related to mass conservation. To analyze this more deeply, we first recall that the mass of ice on the domain is defined as*

$$m = \int \rho\, h\, dx$$

where ρ is the constant sea ice density. We then define the discrete scaled mass *at arbitrary time*

level n as

$$\widehat{m} = \frac{\sum_{j=1}^{N} h^n_{j-\frac{1}{2}}}{\sum_{j=1}^{N} h^0_{j-\frac{1}{2}}} \times 100\%. \tag{5.6}$$

We note that (5.6) *describes the percentage of discrete scaled mass to indicate the deviation from the true amount.*

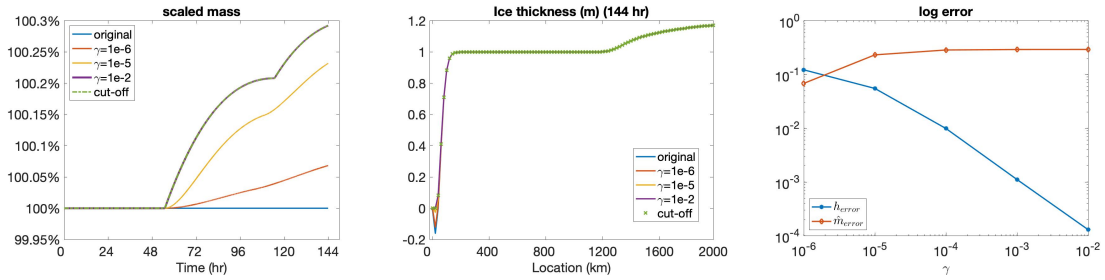

Figure 4: Potential function method example. (Left) scaled mass (5.6); (middle) ice thickness at final time; (right) log of ice thickness error and scaled mass error as a function of γ in (5.5).

Figure 4(left) presents the scaled mass $\widehat{m}$ in (5.6) *as a function of time obtained using (1) the scheme without employing the potential function method or the cut-off method (referred to as "original" in each figure), (2) the scheme with the potential function method* (4.6) *applied to the h transport equation, using different choices for γ in* (5.5)*, and (3) the scheme with cut-off post-processor. To avoid unintended effects due to the equations being coupled, we choose $\gamma_1 = \gamma_2 = 0$ (i.e. we do not adopt the potential function method for A going out of range). Observe that, as expected, mass is conserved when neither the cut-off nor the potential function method is used on top of the currently adopted numerical scheme, while employing either causes an increase in the scaled mass percentage. This artificial mass gain is more pronounced when larger parameters are used in the potential function method. Using the cut-off post-processor results in similar behavior. Conversely, as observed in Figure 4(middle) the larger parameters in the potential method reduce the out-of-range problem near $h = 0$, with similar behavior once again observed for the cut-off post-processor. To quantify this trade-off relationship, we define*

$$h_{error} = \max_t |0 - \min\{0, \min_x h\}| = \max_t |\min\{0, \min_x h\}|$$

which measures the out-of-range error for h, and

$$\widehat{m}_{error} = \max_t |100\% - \widehat{m}|$$

which measures the mass conservation discrepancy. Note that we write h_{error} in this form to emphasize that we are measuring the discrepancy between the non-physical negative value of ice thickness with 0. Figure 4(right) displays the log_{10} magnitude of these two quantities with respect to the parameter γ in the potential function method and verifies the trade-off between out-of-range errors and scaled mass percentage errors.

5.4. Comparison with the reference scheme

This numerical test is designed to compare the proposed method (WENO TVDRK3 with potential function method) with the reference scheme (see paragraph above Section 4.1.1). The model domain is 2000 km long and the total simulation time is 6 days. The experiment is initialized with three types of ice block on the domain given by

$$\begin{aligned} u &= 0 \text{ m/s} \quad \text{on} \quad [0, 2000] \text{ km}, \\ h &= \begin{cases} 1.2 \text{ m} & \text{on} \quad [0, 800] \text{ km}, \\ 0.5 \text{ m} & \text{on} \quad [800, 1600] \text{ km}, \\ 1.2 \text{ m} & \text{on} \quad [1600, 2000] \text{ km}, \end{cases} \\ A &= \begin{cases} 0.8 & \text{on} \quad [0, 800] \text{ km}, \\ 0.5 & \text{on} \quad [800, 1600] \text{ km}, \\ 0.9 & \text{on} \quad [1600, 2000] \text{ km}. \end{cases} \end{aligned} \tag{5.7}$$

Homogeneous Dirichlet boundary conditions (5.4) are imposed. A "ramp-up" type of wind forcing is imposed as the only external forcing term. That is, the wind is chosen to be gradually increasing temporally as $u_a(t) = 10\,(1 - e^{-t/\tau})$ m/s with τ being set to six hours and remain uniform pattern spatially. The simulation is run with a spatial resolution of $\Delta x = 20$ km. As for the time step, we use $\Delta t = 1$ s for the proposed method and $\Delta t = 300$ s for the reference scheme. [6]

[6] Since our proposed method uses explicit time-stepping to solve (2.2a), a small time step is needed to ensure numerical stability. This restriction may be alleviated by either using an implicit time-stepping method or an EVP

Figure 5 shows solutions for u, h and A at the final time of 6 days along with the scaled mass percentage (5.6) obtained by each method with and without treatment of non-physical values (the potential function method and cut-off post-processor, respectively). We note that the WENO scheme does not yield non-physical negative solutions for either A or h, so that we need only apply the potential function method to treat non-physical solutions for $A > 1$. In this case we choose $\gamma_2 = 10^{-2}$. Observe that while the velocity profiles behave similarly for the reference and proposed method, as well as for when the respective treatments are included, it is clear that only our proposed method maintains a sharp non-oscillatory solution in each sub-region for the ice thickness and ice concentration. As desired, applying the potential function method helps to nudge the non-physical value for ice concentration A back into range, which results in a clear ridging effect near the right boundary (by correcting the artificial numerical solutions) for ice velocity u and ice thickness h. On the other hand, the reference scheme generates sharp overshoots in both the ice thickness and ice concentration profiles. The cut-off post-processor mitigates these overshoots but does not completely resolve the issue. Finally, while neither method maintains mass conservation, the discrepancy seen in the proposed method is clearly less than for the reference scheme. In this regard, it is interesting to observe that in the long term, using the cut-off post-processor (as applied to the reference scheme) appears to cause greater conservation discrepancy than using the potential function method in conjunction with the proposed method.

6. Concluding remarks

This paper discusses the current methodology and limitations, namely poor convergence and out-of-range issues for both ice concentration and ice thickness, for solving the VP sea ice model. To improve the performance of the numerical solutions, we propose the use of higher-order methods. In particular, a case study of the celebrated WENO scheme is provided for the 1D sea ice model, and we verify its improved numerical convergence when compared to standardly employed algorithms. Moreover, WENO is able to resolve discontinuities and sharp features that may occur

model. Implicit time-stepping methods for WENO schemes have been studied in [42, 43], and we will consider these approaches in future work. As previously discussed (see Remark 3.3), the purpose of this investigation is to analyze convergence with respect to spatial resolution, so the time step here is simply chosen to avoid additional temporal error.

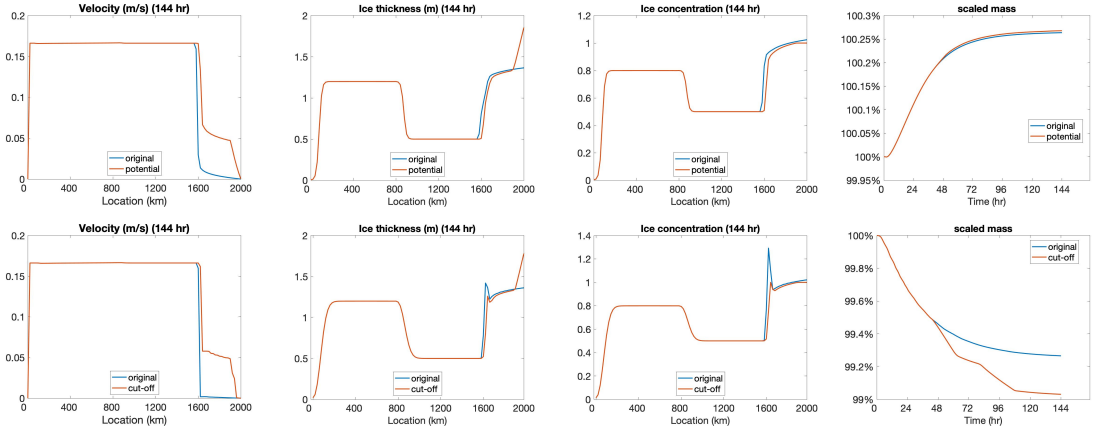

Figure 5: Comparison between the proposed method and reference scheme. (Top) solution plots and scaled mass using the proposed method, with and without potential function method; (bottom) solution plots and scaled mass using reference scheme, with and without cut-off post-processor. (From left to right) velocity u, ice thickness h, ice concentration A, and scaled mass percentage $\widehat{m}$.

in sea ice covers. With regard to the out-of-range issue, this investigation proposes and implements a potential function method that naturally incorporates the physical restrictions of ice thickness and ice concentration in the transport equations.

Since it is relatively easier to examine numerical convergence properties, the current work is restricted to a 1D case study. Moving forward, we will test the ideas here of using both higher-order methods and the potential function approach in more realistic environments, including the 2D model as well as physical set-up test regimes. While direct generalization of the WENO scheme to 2D models is possible, special attention must be paid to the boundary treatment. The ghost-point values extrapolated in the 1D case for the ocean-land boundary can be extended to 2D. Stable extrapolation method of suitable orders of accuracy can also be used for outflow boundaries [44]. Stable high order extrapolation for inflow boundaries is known to be more challenging, however, with some techniques discussed in [20].

In this investigation, the WENO scheme serves as a prototype to demonstrate the benefits of using higher-order methods that are designed to resolve the discontinuities. Other higher-order methods can also be adopted for the 2D case. The discontinuous Galerkin (DG) method is particularly suitable for complex geometries.

Besides viscous-plastic rheology, other rheologies have also been proposed, such as elastic-

anisotropic-plastic rheology [8] and Maxwell elasto-brittle rheology [9]. Investigating the numerical performance of the approaches used here may benefit the numerical solutions for these types of rheologies as well. Another avenue for future work is to obtain a more realistic setup of the sharp features in the sea ice cover by incorporating available observations with the physical model via data assimilation techniques. For example, in [45] data assimilation experiments are based on the 1D VP model discretized by a centered difference scheme, and in future investigations, we can adapt this approach to the higher-order method framework discussed here. Finally, sparse features in the ice thickness have been observed in [45], leading to the successful implementation of an $\ell_1 - \ell_2$ regularization approach. A general framework for incorporating ℓ_1 regularization into numerical solvers for partial differential equations with sparse solutions was developed in [46], and combining ideas from there along with the results here may also be beneficial within the data assimilation framework.

References

[1] M. Parno, B. West, A. Song, T. Hodgdon, D. O'Connor, Remote measurement of sea ice dynamics with regularized optimal transport, Geophysical Research Letters 46 (2019) 5341––5350. doi:10.1029/2019GL083037.

[2] Q. Wang, L. Ju, Y. Xue, Chapter 13 - the application of peridynamics for ice modeling, in: E. Oterkus, S. Oterkus, E. Madenci (Eds.), Peridynamic Modeling, Numerical Techniques, and Applications, Elsevier Series in Mechanics of Advanced Materials, Elsevier, 2021, pp. 275–308. doi:10.1016/B978-0-12-820069-8.00002-0.

[3] E. C. Hunke, W. H. Lipscomb, A. K. Turner, Sea-ice models for climate study: retrospective and new directions, Journal of Glaciology 56 (200) (2010) 1162–1172. doi:10.3189/002214311796406095.

[4] W. D. Hibler, A dynamic thermodynamic sea ice model, Journal of Physical Oceanography 9 (4) (1979) 815 – 846. doi:10.1175/1520-0485(1979)009<0815:ADTSIM>2.0.CO;2.

[5] E. C. Hunke, J. K. Dukowicz, An elastic–viscous–plastic model for sea ice dynamics, Journal of Physical Oceanography 27 (9) (1997) 1849 – 1867. doi:10.1175/1520-0485(1997)027<1849:AEVPMF>2.0.CO;2.

[6] E. C. Hunke, Viscous–plastic sea ice dynamics with the EVP model: Linearization issues, Journal of Computational Physics 170 (1) (2001) 18–38. doi:10.1006/jcph.2001.6710.

[7] L. Girard, S. Bouillon, J. Weiss, D. Amitrano, T. Fichefet, V. Legat, A new modeling framework for sea-ice mechanics based on elasto-brittle rheology, Annals of Glaciology 52 (57) (2011) 123–132. doi:10.3189/172756411795931499.

[8] A. V. Wilchinsky, D. L. Feltham, Modelling the rheology of sea ice as a collection of diamond-shaped floes, Journal of Non-Newtonian Fluid Mechanics 138 (1) (2006) 22–32. doi:10.1016/j.jnnfm.2006.05.001.

[9] V. Dansereau, J. Weiss, P. Saramito, P. Lattes, A Maxwell elasto-brittle rheology for sea ice modelling, The Cryosphere 10 (3) (2016) 1339–1359. doi:10.5194/tc-10-1339-2016.

[10] C. F. Ip, W. D. Hibler, G. M. Flato, On the effect of rheology on seasonal sea-ice simulations, Annals of Glaciology 15 (1991) 17–25. doi:10.3189/1991AoG15-1-17-25.

[11] J.-F. Lemieux, B. Tremblay, J. Sedláček, P. Tupper, S. Thomas, D. Huard, J.-P. Auclair, Improving the numerical convergence of viscous-plastic sea ice models with the Jacobian-free Newton–Krylov method, Journal of Computational Physics 229 (8) (2010) 2840–2852. doi:10.1016/j.jcp.2009.12.011.

[12] R. Kwok, E. C. Hunke, W. Maslowski, D. Menemenlis, J. Zhang, Variability of sea ice simulations assessed with RGPS kinematics, Journal of Geophysical Research: Oceans 113 (C11) (2008). doi:10.1029/2008JC004783.

[13] J.-F. Lemieux, B. Tremblay, Numerical convergence of viscous-plastic sea ice models, Journal of Geophysical Research: Oceans 114 (C5) (2009). doi:10.1029/2008JC005017.

[14] J.-F. Lemieux, D. Knoll, B. Tremblay, D. Holland, M. Losch, A comparison of the Jacobian-free Newton–Krylov method and the EVP model for solving the sea ice momentum equation with a viscous-plastic formulation: A serial algorithm study, Journal of Computational Physics 231 (17) (2012) 5926–5944. doi:10.1016/j.jcp.2012.05.024.

[15] M. Kimmritz, S. Danilov, M. Losch, On the convergence of the modified elastic–viscous–plastic method for solving the sea ice momentum equation, Journal of Computational Physics 296 (2015) 90–100. doi:10.1016/j.jcp.2015.04.051.

[16] J.-F. Lemieux, D. A. Knoll, M. Losch, C. Girard, A second-order accurate in time IMplicit–EXplicit (IMEX) integration scheme for sea ice dynamics, Journal of Computational Physics 263 (2014) 375–392. doi:10.1016/j.jcp.2014.01.010.

[17] J. Williams, L. B. Tremblay, The dependence of energy dissipation on spatial resolution in a viscous-plastic sea-ice model, Ocean Modelling 130 (2018) 40–47. doi:10.1016/j.ocemod.2018.08.001.

[18] C. Seinen, A fast and efficient solver for viscous-plastic sea ice dynamics, Master's thesis, University of Victoria (2017).

[19] C. Seinen, B. Khouider, Improving the jacobian free newton–krylov method for the viscous–plastic sea ice momentum equation, Physica D: Nonlinear Phenomena 376-377 (2018) 78–93, special Issue: Nonlinear Partial Differential Equations in Mathematical Fluid Dynamics. doi:10.1016/j.physd.2017.09.005.

[20] C.-W. Shu, Essentially non-oscillatory and weighted essentially non-oscillatory schemes, Acta Numerica 29 (2020) 701–762. doi:10.1017/S0962492920000057.

[21] X.-D. Liu, S. Osher, T. Chan, Weighted essentially non-oscillatory schemes, Journal of Computational Physics 115 (1) (1994) 200–212. doi:10.1006/jcph.1994.1187.

[22] D. Kuzmin, A Guide to Numerical Methods for Transport Equations, Friedirch-Alexander Universitäte Erlangen-Nürnberg, 2010.

[23] A. S. Thorndike, D. Rothrock, G. Maykut, R. Colony, The thickness distribution of sea ice, Journal of Geophysical Reseach 80 (33) (1975) 4501–4513. doi:10.1029/JC080i033p04501.

[24] E. Hunke, W. Lipscomb, A. Turner, N. Jeffery, S. Elliott, CICE: the Los Alamos sea ice model documentation and software user's manual version 5.1 (2015).

[25] C. Mehlmann, Efficient numerical methods to solve the viscous-plastic sea ice model at high spatial resolutions, Ph.D. thesis, Otto-von-Guericke-Universität Magdeburg, Fakultät für Mathematik (2019).

[26] W. H. Lipscomb, E. C. Hunke, Modeling sea ice transport using incremental remapping, Monthly Weather Review 132 (6) (2004) 1341 – 1354. doi:10.1175/1520-0493(2004)132<1341:MSITUI>2.0.CO;2.

[27] G. Fix, Phase field models for free boundary problems, in: A. Fasano, M. Primicerio (Eds.), Free Boundary Problems: Theory and Applications, Vol. 2, Boston: Pitman, 1983, p. 580.

[28] J. S. Langer, Models of pattern formation in first-order phase transitions, in: Directions in Condensed Matter Physics, Singapore: World Scientific, 1986, pp. 165–186. doi:10.1142/9789814415309_0005.

[29] J. Zhang, W. D. Hibler III, On an efficient numerical method for modeling sea ice dynamics, Journal of Geophysical Research: Oceans 102 (C4) (1997) 8691–8702. doi:10.1029/96JC03744.

[30] W. H. Lipscomb, E. C. Hunke, W. Maslowski, J. Jakacki, Ridging, strength, and stability in high-resolution sea ice models, Journal of Geophysical Research: Oceans 112 (C3) (2007). doi:10.1029/2005JC003355.

[31] M. McPhee, Ice-ocean momentum transfer for the AIDJEX ice model, in: AIDJEX Bulletin, Vol. 29, University of Washington, 1975, pp. 93–111.

[32] J. Williams, L. B. Tremblay, J.-F. Lemieux, The effects of plastic waves on the numerical convergence of the viscous–plastic and elastic–viscous–plastic sea-ice models, Journal of Computational Physics 340 (2017) 519–533. doi:10.1016/j.jcp.2017.03.048.

[33] K. E. Atkinson, An Introduction to Numerical Analysis, John Wiley & Sons, 1989.

[34] Y. Saad, A flexible inner-outer preconditioned GMRES algorithm, SIAM Journal on Scientific Computing 14 (2) (1993) 461–469. doi:10.1137/0914028.

[35] S. C. Eisenstat, H. F. Walker, Choosing the forcing terms in an inexact Newton method, SIAM Journal on Scientific Computing 17 (1) (1996) 16–32. doi:10.1137/0917003.

[36] J.-F. Lemieux, B. Tremblay, S. Thomas, J. Sedláček, L. A. Mysak, Using the preconditioned generalized minimum residual (GMRES) method to solve the sea-ice momentum equation, Journal of Geophysical Research: Oceans 113 (C10) (2008). doi:10.1029/2007JC004680.

[37] J.-P. Auclair, J.-F. Lemieux, L. Tremblay, H. Ritchie, Implementation of Newton's method with an analytical Jacobian to solve the 1D sea ice momentum equation, Journal of Computational Physics 340 (2017) 69–84. doi:10.1016/j.jcp.2017.02.065.

[38] C.-W. Shu, S. Osher, Efficient implementation of essentially non-oscillatory shock-capturing schemes, Journal of Computational Physics 77 (2) (1988) 439–471. doi:10.1016/0021-9991(88)90177-5.

[39] Y. Liu, C.-W. Shu, M. Zhang, High order finite difference WENO schemes for nonlinear degenerate parabolic equations, SIAM Journal on Scientific Computing 33 (2) (2011) 939–965. doi:10.1137/100791002.

[40] G.-S. Jiang, C.-W. Shu, Efficient implementation of weighted ENO schemes, Journal of Computational Physics 126 (1) (1996) 202–228. doi:10.1006/jcph.1996.0130.

[41] A. Arakawa, V. Lamb, Computational design of the basic dynamical processes of the UCLA general circulation model, in: J. CHANG (Ed.), General Circulation Models of the Atmosphere, Vol. 17 of Methods in Computational Physics: Advances in Research and Applications, Elsevier, 1977, pp. 173–265. doi:10.1016/B978-0-12-460817-7.50009-4.

[42] A. Cadiou, C. Tenaud, Implicit WENO shock capturing scheme for unsteady flows. Application to one-dimensional Euler equations, International Journal for Numerical Methods in Fluids 45 (2) (2004) 197–229. doi:10.1002/fld.685.

[43] S. Gottlieb, J. S. Mullen, S. J. Ruuth, A fifth order flux implicit WENO method, Journal of Scientific Computing 27 (2006) 271–287. doi:10.1007/s10915-005-9034-z.

[44] M. Goldberg, On a boundary extrapolation theorem by Kreiss, Mathematics of Computation 31 (138) (1977) 469–477. doi:10.2307/2006427.

[45] N. Asadi, K. A. Scott, D. A. Clausi, Data fusion and data assimilation of ice thickness observations using a regularisation framework, Tellus A: Dynamic Meteorology and Osceanography 71 (1) (2019) 1564487. doi:10.1080/16000870.2018.1564487.

[46] T. Scarnati, A. Gelb, R. B. Platte, Using ℓ_1 regularization to improve numerical partial differential equation solvers, Journal of Scientific Computing 75 (1) (2018) 225–252. doi:10.1007/s10915-017-0530-8.

Appendix A. A simulation of sea ice with sharp features for the EVP model

Our investigation focuses on the VP model. Since the EVP model is designed for explicit time-stepping and is often used in practice, here we conduct a test to determine how well the WENO scheme performs when using the EVP. For this purpose we consider the simulation of the sea ice cover with sharp features as discussed in Section 5.2. In addition to demonstrating that WENO can indeed be incorporated into the EVP model, we moreover observe that in doing so we are able to resolve the sharp features near the discontinuity region, just as for the VP model. Furthermore, while the WENO spatial discretization scheme is complemented with the explicit time stepping scheme (TVDRK3), the EVP model (see Section 3.2) relaxes the stability condition so that a larger time step can be used. Thus in this experiment we run the simulation with spatial resolution $\Delta x = 10$ km and time step $\Delta t = 10$ s with 1000 sub-cycling steps for a total simulation time of 1 hour.

As in Figure 1 in Section 5.2, Figure A.6 displays the solution for the initial conditions given in (5.3) obtained by WENO (top row), linear WENO (middle row) and CD (bottom row) spatial discretizations. Once again, the simulation can only reach the final time of 1 hour using the WENO scheme. Observe that the results for the EVP and VP models are nearly identical, with no oscillatory behavior near discontinuities. The linear WENO solution is shown at time 2110 s, where again we see oscillations in the velocity profile. The bottom row (left) shows the velocity during the sub-cycling iteration between 2340 s and 2350 s. The ice thickness and ice concentration at 2340 s are shown in the bottom-middle and bottom-right, respectively. We present the velocity profile during the sub-cycling stage to capture the undershoot that occurs within the sub-cycling – it is not detectable outside the sub-cycling for this case. This undershoot eventually leads to the solution blowing up before reaching the final time.

This simulation result further verifies that for both the VP and EVP models, the WENO scheme properly resolves discontinuities and obtains a stable solution. By contrast, neither the CD nor the traditional higher-order (linear WENO) schemes provide satisfactory results in either case.

Appendix B. The fifth-order WENO scheme

WENO schemes are designed to obtain high order accuracy in smooth regions while sharply resolving discontinuities. By adapting the stencil of the given grid-points to be more one-sided near

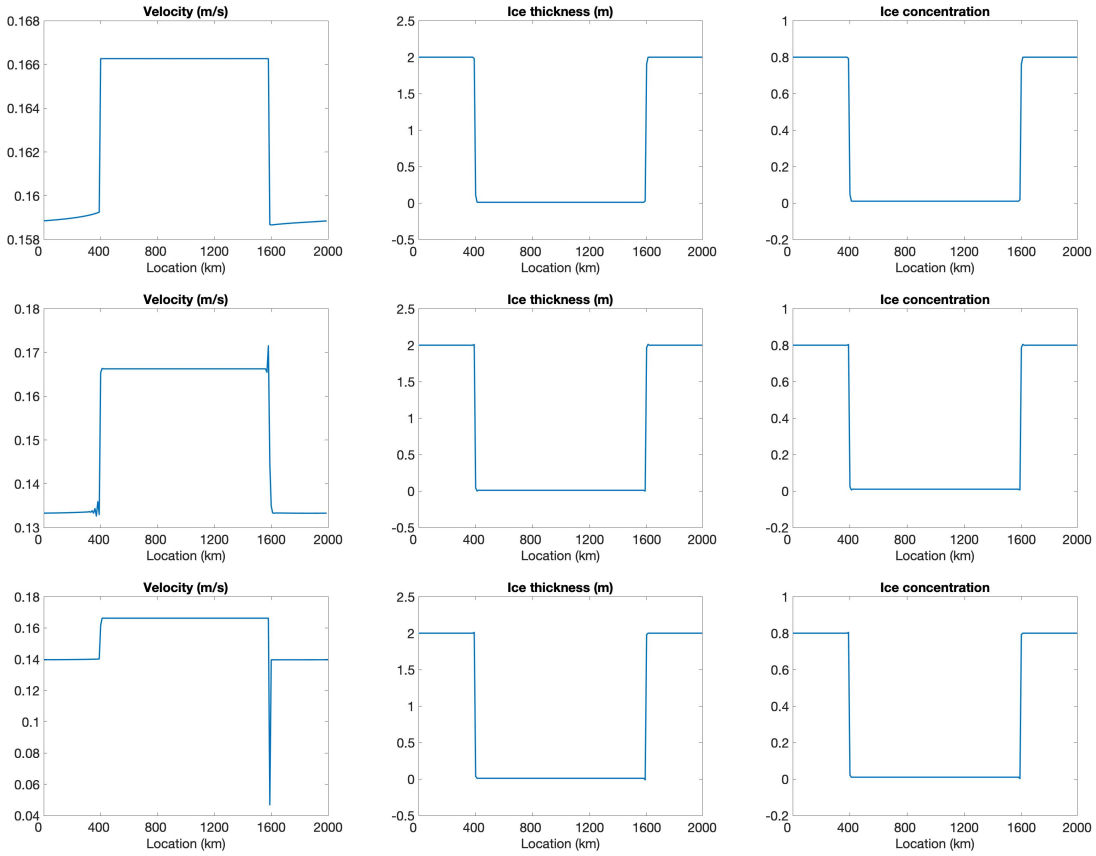

Figure A.6: Simulation of sea ice with sharp features on EVP model. (Top) solution plots of u, h and A using WENO at 1 hour; (middle row) solution plots of u, h and A using linear WENO at 2110 s; (bottom) solution plots of u (left) during sub-cycling between 2340 s and 2350 s; h (middle) at 2340 s; A (right) at 2340 s using CD .

discontinuities, WENO is a modification of the celebrated *essentially non-oscillatory* (ENO) scheme, [38]. Originally designed to solve hyperbolic and convection-diffusion equations, they have been extensively generalized and adapted for different types of PDEs as well as to non-PDE problems. Below we briefly describe the basic ideas based on the most commonly used fifth-order WENO scheme in [40] for the 1D scalar conservation law for some generic variable z given by

$$\frac{\partial z}{\partial t} + \frac{\partial}{\partial x} f(z) = 0, \tag{B.1}$$

with appropriate initial and boundary conditions for $x \in [a, b]$ and $t > 0$.

The domain is discretized with uniform grid points $\{x_j\}_{j=1}^{N}$ so that $x_j = a + j\Delta x$. We seek the

numerical approximation $z_j(t)$ to the point value $z(x_j, t)$ using the conservative scheme

$$\frac{\partial z_j}{\partial t} + \frac{1}{\Delta x}\left(\widehat{f}_{j+\frac{1}{2}} - \widehat{f}_{j-\frac{1}{2}}\right) = 0, \tag{B.2}$$

where the numerical flux function

$$\widehat{f}_{j+\frac{1}{2}} = \widehat{f}(z_{j-r}, \cdots, z_{j+s})$$

is chosen so that the conservative difference $\widehat{f}_{j+\frac{1}{2}} - \widehat{f}_{j-\frac{1}{2}}$ approximates $\frac{\partial}{\partial x} f(z)$ at $x = x_j$ with high order accuracy in smooth regions while also generating an essentially non-oscillatory solution near discontinuities.

Flux splitting techniques, such as the global Lax-Friedrichs (LF) flux splitting, are used for general flux $f'(x) \ngeq 0$, with

$$\widehat{f}_{j+\frac{1}{2}} = \widehat{f}^{+}_{j+\frac{1}{2}} + \widehat{f}^{-}_{j+\frac{1}{2}}. \tag{B.3}$$

In particular, the fifth-order WENO procedure computes $\widehat{f}^{+}_{j+\frac{1}{2}}$ based on the left-biased "big" stencil

$$S = \{x_{j-2}, \cdots, x_{j+2}\}$$

by forming a convex combination of three third-order ENO candidate polynomials

$$\widehat{f}^{+}_{j+\frac{1}{2}} = \sum_{m=0}^{2} \omega_m \widehat{f}^{(m)}_{j+\frac{1}{2}}. \tag{B.4}$$

Each ENO candidate polynomial $\widehat{f}^{(m)}_{j+\frac{1}{2}}$ in (B.4) is a lower-order linear scheme constructed from a "small" stencil

$$S^m = \{x_{j-2+m}, x_{j-1+m}, x_{j+m}\},$$

while ω_m, $m = 0, \ldots, 2$, are the corresponding nonlinear weights designed to maintain high order accuracy in smooth regions and yield non-oscillatory solutions near discontinuities. Note that for smooth solutions, the nonlinear weights ω_m are equivalent to the linear weights for which the highest possible accuracy (in this case fifth-order) could be achieved. We refer to [40] for more details. A thorough review on ENO and WENO schemes is available in [20] with particular extension for parabolic equations in [39].